Application of random lasers for multi-scale dynamics process in the nanomicroscale

Nideesh Padiyakkuth, Nandakumar Kalarikkal, Rodolphe Antoine

CHAPTER 12

Application of random lasers for multi-scale dynamics process in the nano-microscale

Nideesh Padiyakkuth[a], Nandakumar Kalarikkal[a b] and Rodolphe Antoine[c *].

[a]School of Pure and Applied Physics, Mahatma Gandhi University, Priyadarsini Hills P O, Kottayam-686560, India

[b]University Centre for Ultrafast Studies, Mahatma Gandhi University,

Kottayam-686 560, Kerala, India

[c]Institut Lumière Matière UMR 5306, Univ Lyon, Université Claude Bernard Lyon 1, CNRS, F-69100 Villeurbanne, France.

*corresponding email address: rodolphe.antoine@univ-lyon1.fr

ABSTRACT/WEB SUMMARY

12.1 Introduction

Laser technology stands as a monumental achievement in scientific research, renowned for its remarkable light amplification capabilities.[1] The two key ingredients of a conventional laser are an active material for light amplification and a feedback mechanism for confinement, which have long been the gold standard. But what if we could think of a feedback mechanism without mirrors? There enters the mirrorless lasing [2–5], an alternative proposal put forth by Letokhov.[6]

Lasing is a process of stimulated emission of light by a gain medium, typically a material with an inverted population of excited atoms or molecules. It is characterized by coherent and monochromatic light emission and typically requires a feedback mechanism to sustain amplification. This feedback mechanism is provided by an optical cavity, typically composed of two mirrors. Random lasing is an alternative approach to conventional lasing, which can occur in a disordered medium without the need for a well-defined cavity or mirrors. Here, light is amplified through multiple scattering events in the medium, leading to a complex interplay between coherent feedback and random scattering. Random laser (RL) only requires a gain medium and a disordered scattering medium for optical amplification and feedback respectively. Random lasing has been observed in a wide range of materials, including powders[7–10], polymers [11–14], and biological tissues .[15–19] Random lasing holds potential for a wide range of applications, including sensing [20,21], imaging[17,22,23], and RL-based therapy[24], and continues to be an active area of research in the field of photonics. Traditionally, scattering is viewed as a harmful element that causes cavity loss, but recent findings have shown that strong scattering can generate lasing-like phenomena with astonishing benefits. By using a disordered medium called a random media, which contains multiple scattering

centers, photons encounter multiple scattering and increase their dwell time in the medium. Consequently, the efficiency of light amplification is enhanced. The low spatial coherence of RLs makes them ideal for a wide range of applications, including cancer diagnostics[16,18], photonic barcodes[25], sensing, and optomicrofluidics.[26,27]

Speckle imaging is a technique that utilizes coherent light, such as a laser, to capture images of objects. The resulting image shows variations in intensity and color, known as speckle patterns, which are caused by the interference of scattered light waves from the surface of the object. Speckle imaging has diverse applications in fields such as astronomy, microscopy, and remote sensing. Conversely, speckle-free imaging[28–30] is a method that aims to remove or reduce these speckle patterns in order to enhance image quality. This technique employs a random medium, such as a disordered scattering medium, to generate a RL. The RL emits light with low spatial coherence, which results in averaging out the speckle patterns, leading to a coherent artifact-free image. Speckle-free imaging is beneficial in biomedical imaging, where it enables obtaining clear images of tissues and organs. Therefore, this chapter presents an overview of random lasing in the context of speckle-free imaging applications.

12.2 Pump-probe optical microscopy for multi-scale dynamics process in the nano-microscale. Coherence and Speckles.

The pump-probe optical microscopy setup described in this chapter was developed by the group of Razvan Stoian in Saint-Etienne, France.[31] This setup was adapted to study the formation of bubbles generated by laser-induced cavitation.[32] The

experimental setup with a time-resolved pump-probe observation is displayed in Figure 12.1.

12.2.1. Bessel beam generation

An ultra-fast amplified Ti: Sapphire laser is used as the illumination system. The laser pulse duration is 60 fs and is centered at 800 nm with a repetition rate of 1 kHz (Legend, Coherent). Single pulse generation is possible through a system of optoelectronic and mechanical shutters. The time envelope of the pulses can be controlled from 60 fs to a few picoseconds via the compressor. Depending on the laser firing conditions, the energy of a pulse is a few tens of µJ.

Among the various methods for generating non-diffracting beams by conical intersection, the zero-order of a Bessel beam has been used.[33,34] This is a narrow and intense “non-propagating” laser beam generated from a Gaussian beam by an axicon lens (the angle of the axicon tip is 179°). The core of the Bessel beam is expanded and then focused into the sample using a 4f afocal imaging system with a microscope lens as the final imaging element. Spatial filtering was used to avoid losses due to the axicon tip.[35]

12.2.2. Time-resolved microscopy

The observation is done by optical microscopy using a two-color time-resolved pump-probe system. The imaging setup is based on an upright optical microscope (Olympus BX-51) operating in diascopic transmission or phase contrast illumination mode. In optical transmission microscopy, the scattering or absorbing regions appear dark on a light background. In phase contrast microscopy, changes in the

phase of the probe beam induced by a change in the refractive index of the sample Δn negative (respectively Δn positive) appear bright (respectively dark) or on a grey background.

For the pump-probe imaging technique, the pulsed laser beam is split into two by a beam splitter. The pump beam at 800nm is used for plasma generation in the sample, and the probe beam is used for imaging. The frequency of the probe beam is doubled by the Second Harmonic Generation (SHG) with a β barium borate (BBO) crystal. The optical path of the probe beam (delay line) is different from that of the pump beam: the control of the length of this optical path makes it possible to induce a delay between the generation of the plasma (the pump) and the acquisition of the image of the sample (the probe) with a precision of the order of a picosecond. A motorised translation stage controls this time delay. This technique then allows a dynamic analysis resolved in time by a stroboscopic illumination.

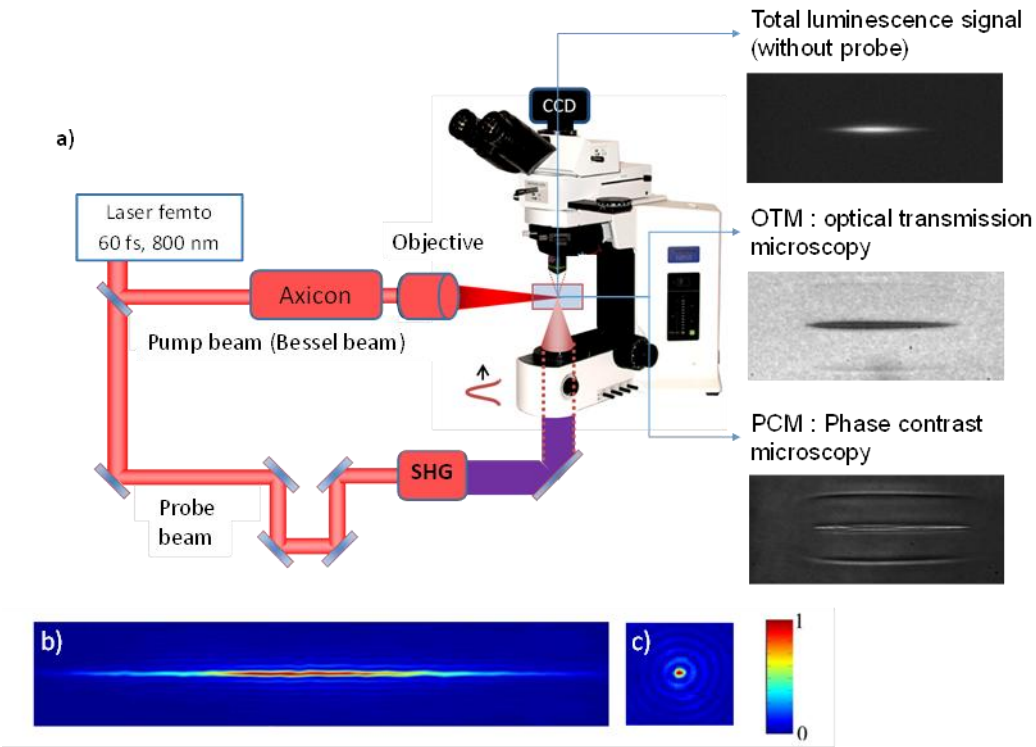

Figure 12.1 (a) Experimental setup with a time-resolved pump-probe observation. Simulation of the intensity of a Bessel beam projected (b) along the propagation axis and (c) in a plane transverse to the propagation axis of the laser beam.

The sample is imaged perpendicular to the excitation axis (i.e., the pump beam propagates horizontally and the probe beam vertically) using a Köhler illumination technique, giving us information on both the amplitude and the phase of the signal. The use of a diffuser mounted in the optical path of the probe beam reduces its spatial coherence, thus increasing the uniformity of the illumination. The probe beam enters the microscope through the microscope condenser. Images (optical transmission microscopy and phase contrast microscopy) are recorded in the image focal plane by an EMCCD camera with electronic backlighting.

The spatial and temporal coherence of the probe beam induces the presence of luminous spots, also called “speckles” or “hot spots”, which are dramatic to image single-shot acquisition, as shown in Figure 12.2. Thus, for correct imaging quality, 50 acquisitions are required to be superimposed to obtain a correct image. This random artifact originates from the coherent character of the laser beam used for illumination. Indeed, despite the diffuser used to diminish the high spatial coherence of the probe beam, this phenomenon is due to interference between the rays scattered by each point of the observed sample. In order to be able to perform image acquisition on a single laser shot, the need to develop a new, intense, non-coherent, pulsed illumination source comes naturally.

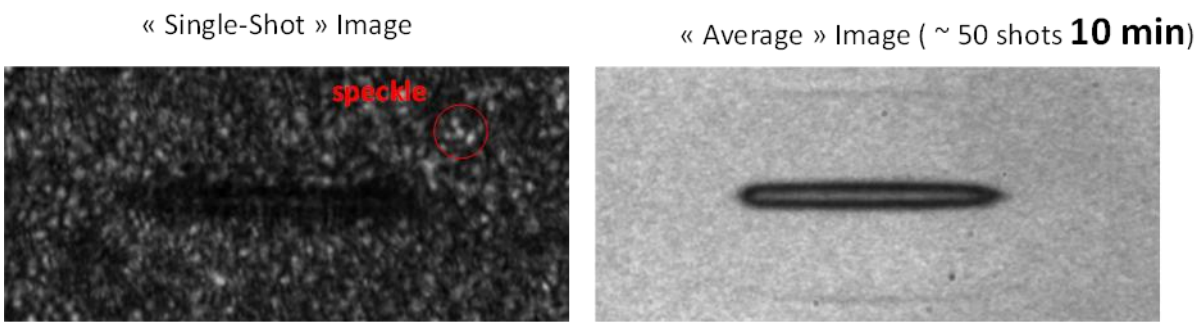

Figure 12.2 Image of the micrometric bubble obtained after a single laser shot (a single acquisition) and averaged over 50 shots, illustrating the problem of spatial and temporal coherence of the probe beam inducing “speckles”.

12.2.3. Random laser. An ideal light source for speckle-free imaging

The variety of light sources is large. These sources can be classified according to their intensity and spatial coherence (Figure 12.3). For example, incandescent lamps are known for their simplicity. The thermal nature of light, by blackbody radiation, imposes a spatial decoherence of the light wave trains. However, the luminous intensity of these lamps is very low, especially when pulsed illumination of the order of a few nanoseconds is desired. Lasers or super-luminescent diodes are particularly intense, but by construction their emission is highly coherent.[23] There are a number of pulsed light sources with high intensity and low spatial coherence. One is the use of pulsed diodes, which are being developed more and more intensively in order to achieve sufficient brightness for imaging.[36] But, in general, this instrumentation remains either very expensive or not efficient enough for optical microscopy, which requires significant illumination of the sample. On the other hand, flash lamps are based on the emission of a plasma generated by an intense electric arc in a gas. They can reach high light intensities for a pulse duration of about ten nanoseconds.

However, the plasma emission band of flash lamps is very wide, which restricts its field of application when wavelength selection of the emission is desired.

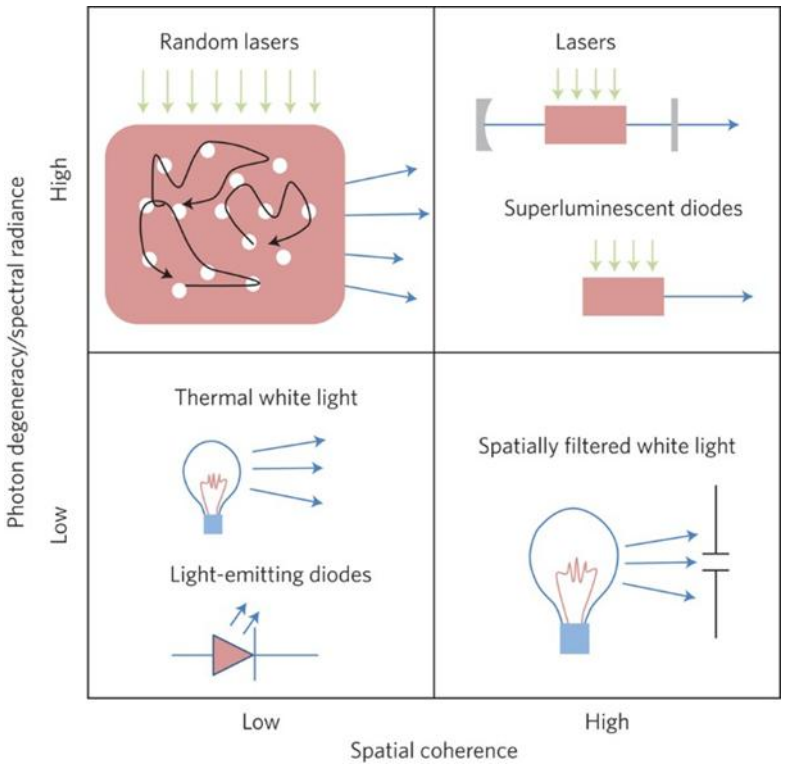

Figure 12.3 Graphical representation of the problem of illumination techniques for optical microscopy.

The RL is an atypical laser technology that has not yet been widely exploited for time-resolved optical imaging.[37] In this section, we will present the basic physical principles of RL emission and then we will review the different families of random lasers (RLs) that have been developed using advanced materials.[38]

12.3. Basic principles of random lasers

Briefly, in laser physics, three basic mechanisms are involved: absorption, spontaneous emission, and stimulated emission. Simplified Jablonski diagrams of these mechanisms are given in Figure 12.4. For the sake of clarity, let us consider a system with four energy levels.

For lasing to occur, it is necessary for the excited state of the laser transition (state 2) to be more populated than its ground state (state 1). To achieve this, energy must be supplied to the system through the absorption of “pump” photons allowing the transition between state 1’ and state 2’. State 2 is then populated by fast non-radiative transitions ($k_{2'2}$) from state 2’, and state 1 is depopulated by fast non-radiative transitions ($k_{11'}$). If the energy input from the pump is sufficiently large (existence of a laser threshold), state 2 remains sufficiently populated for the stimulated emission to be amplified by positive feedback: a photon emitted after spontaneous emission from the transition from state 2 to state 1 can induce a stimulated emission, thus generating two photons, which can, in turn, induce new stimulated emissions, and so on.

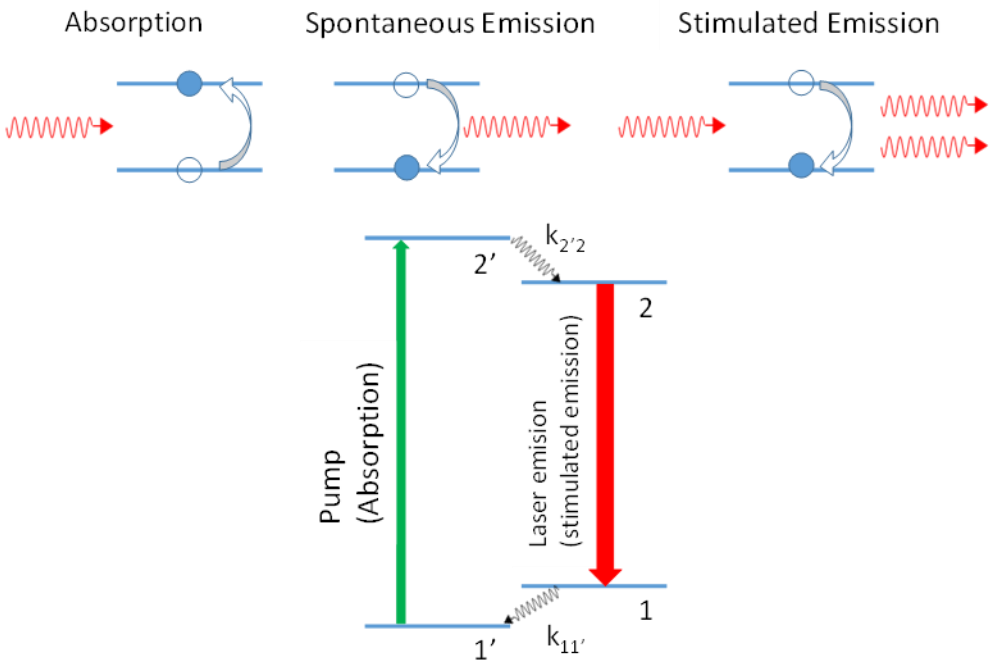

Figure 12.4 Description of the mechanisms involved in the laser process with a simplified Jablonski diagram for a four-level system.

In a conventional laser, this feedback, which allows the stimulated emission to be amplified, is provided by the presence of a resonant optical cavity around the amplifying medium: this is called coherent feedback. By construction, it is the presence of this optical cavity that imposes the coherent character of the laser beam and the laser emission is directional along the axis of the optical cavity (Figure 12.5a).

As predicted by Letokhov et al in 1966[39], the RL is a laser technology without an optical cavity. The amplification of the stimulated emission is then ensured, not by an optical cavity, but by the multiple and random diffusion of photons in a highly disordered amplifying medium. The RL emission occurred in all directions (Figure 12.5b).[40] RLs can be divided into two categories based on the feedback mechanism, (1) Resonant feedback (coherent feedback) in RLs selectively amplifies specific wavelengths through constructive interference of scattered light waves, resulting in pronounced peaks in the laser output spectrum. This mechanism relies on light finding closed-loop paths within the medium. In this type of feedback, the spectrum consists of multiple ultranarrow peaks (attributed as modes in RLs). (2) In contrast, non-resonant feedback (incoherent feedback) utilizes open paths. It leads to a smooth output spectrum due to the amplification of a wider range of frequencies without strong interference effects. Here, the spectrum is characterized by a single smooth narrow peak.

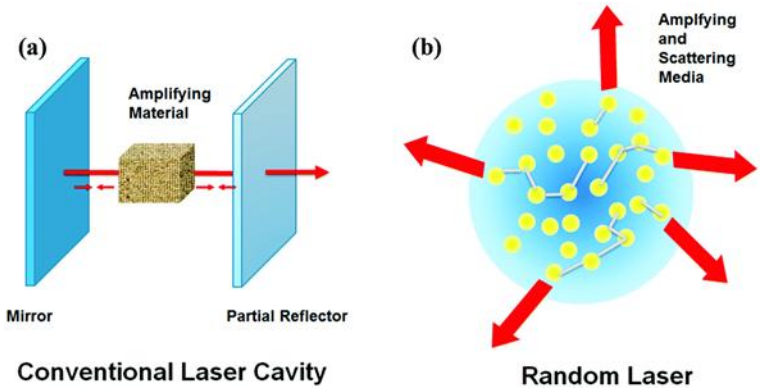

Figure 12.5 On the left, the principle of a “classical” laser. An optical cavity provides feedback. On the right, the principle of a random laser. The feedback is provided by multiple and successive scatterings in the amplifying medium.

The presence of the number of multiple peaks (modes) was found to be highly dependent on the experimental conditions. For instance, reducing the pump spot size or using a pump pulse duration of a picosecond instead of nanosecond induced a transition from incoherent to coherent feedback RL. ADD REF. Zhai, T.; Zhou, Y.; Chen, S.; Wang, Z.; Shi, J.; Liu, D.; Zhang, X. Pulse-duration-dependent and temperature-tunable random lasing in a weakly scattering structure formed by speckles. Phys. Rev. A At. Mol. Opt. Phys. 2010, 82, 23824.

The RLs that are pumped by nanosecond (ns) pulsed lasers usually exhibit incoherent random lasing. However, coherent random lasing can be achieved by using picosecond pulses, which has led to the misconception that picosecond pulses are necessary for coherent random lasing. To dispel this misinterpretation, it is crucial to achieve coherent random lasing based on ns pulses. One promising method to achieve this is by using silver (Ag) nanowires as the scattering source to significantly enhance Raman scattering with different gain materials in the visible range. In this study, the emission properties of a Rhodamine 6G (R6G) laser dye RL with Ag nanowires as the scattering source were investigated. Surprisingly, a

coherent RL pumped by ns pulses was obtained, and emission with coherent spikes was observed at around 575 nm, far from the plasmonic resonance peak of the Ag nanowires at 380 nm. ADD REF DOI: 10.1364/JOSAB.30.002523

12.3.1. Important lengthscales in random lasers

Light localization is typically observed in optical materials with high levels of disorder or randomness, leading to strong scattering processes. To quantitatively describe this phenomenon, it is necessary to introduce two length scales: the scattering mean free path and the transport mean free path. The scattering mean free path[41], denoted as L_S, is the distance between two consecutive scattering events at which the intensity of photon flux is reduced by a factor of 1/e. It can be expressed as $L_s = 1/\rho\sigma_s$, where ρ is the density of particles and σs is the scattering cross-section. The transport mean free path, denoted as L_T, is the average distance traveled by light after which it changes its initial direction or the scattered light is randomized. It can be written as $L_T = 1/\rho\sigma_t$, where σ_t is the transport scattering cross-section. Scattering events can be either isotropic or anisotropic, and for these two cases, there exists a mathematical relationship between scattering and transport mean free paths. Specifically, for isotropic scattering, L_S is proportional to L_T and can be expressed as $L_T = L_S/1-<cos\theta>$, where $<cos\theta>$ is the average cosine of the scattering angle.

To understand amplification in a gain medium, two length parameters are used: the gain length (L_G) and the amplification length (L_A). The gain length measures the distance required for light to be amplified by a factor of e while passing through the medium with scatterers. The amplification length is calculated by taking the root mean square of the distance between the initial and final points of gain length. The

relationship between these two lengths is $L_A = \sqrt{\frac{L_G L_T}{3}}$. If there are no scatterers in the medium, then the gain length is equal to the amplification length. The inelastic length (analogous to L_G), L_I, is the distance over which the intensity of the photon is reduced to 1/e due to absorption. The absorption length parameter (L_{abs}) is the analogous quantity of the amplification length, and it is calculated as $L_{abs} = \sqrt{\frac{L_T L_I}{3}}$. The Ioffe-Regel criterion states that the mean free path of the photons must be smaller than the reciprocal wave vector for photon localization[42]. To characterize the transport regime of a 3D disordered medium, we use the transport mean free path (L_T), wavelength of light (λ), and system size (L). Three major regimes are of interest: (1) The ballistic regime $L_T \geq L$, (2) Diffusive regime $\lambda < L_T < L$, (3) Localization regime $L_T \leq \lambda$.

12.3.2. General considerations and examples for active platforms of RL

Gain media is essential in the development of RLs as it provides the gain necessary for lasing action. Without a gain medium, stimulated emission cannot take place and random lasing cannot occur. Laser dyes and quantum dots are commonly used gain materials in random lasing due to their high fluorescence quantum yield and tunable emission wavelengths. Semiconductors such as ZnO[43–46], ZnS[47-49], and GaAs[50–52] are also used in some experiments due to their large bandgap, which allows for lasing in the blue and UV regions of the spectrum. These materials serve as both gain and scattering media.

TiO_2 nanoparticles are frequently used for colloidal RLs, but their solutions suffer from poor stability. To address this issue, other scatterers such as ZnO, silica, TiO_2-silica core-shell[53,54], alumina[55–57], tungsten oxide[58], nanoclays[59], ferromagnetic

particles[60,61], and polymeric fiber electrospun mats[62], as well as liquid crystals[63–66] have been used.

The refractive index plays a critical role in light scattering in random lasing, as it must be higher than that of the gain medium for effective scattering. In addition, pores within the system structure can also scatter light due to index mismatches. Researchers have utilized porous zirconia[67] and dye-doped hydrogel[68] (as in Figure 12.6) as gain media, with the porous structure serving as a scattering center, enabling tunability and potential for phototherapy. Designing optimal scatterers is crucial for effective random lasing, with recent studies exploring the scattering cross-section of metals and dielectric particles of varying shapes. ZnO nanorods and SiO_2 capped by ZnO nanorod arrays[46,69–71] have been utilized as efficient scatterers in random lasing, offering potential for suppression of spontaneous emission peaks and dominant random lasing peaks.

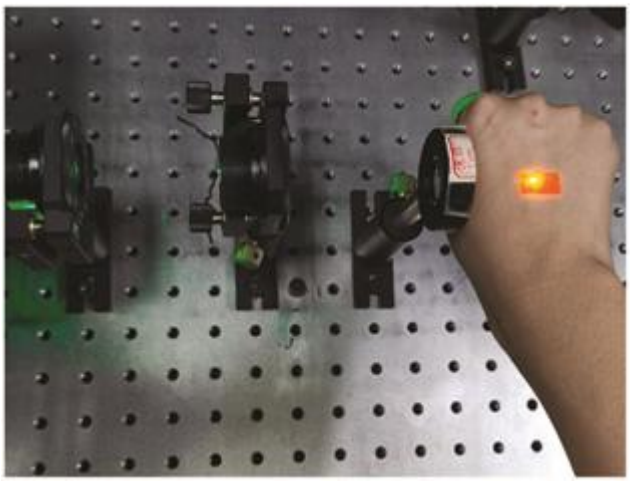

Figure 12.6 Laser pumping experiment of hydrogel attached to the hand.

The use of metal nanoclusters (MNCs) in RLs is an exciting area of research due to their biocompatibility and low toxicity, making them an ideal platform for biomedical applications. One promising approach is integrating highly luminescent MNCs with

hyperbolic metamaterials (HMM) to achieve strong random lasing action with low threshold energy. By using Ag-TSA MNC films (TSA : thiosalicylic acid) as the gain medium and HMM for light trapping, researchers have demonstrated the potential of this approach for RLs.[72] Polymer matrices are also effective as they can serve as a scatterer, gain, or both. Recent studies have also explored the use of biological materials, such as whole blood[73], as the gain medium and SiO_2 as the scatterer. These examples demonstrate the importance of designing RL platforms to achieve optimal conditions for scatterers to achieve excellent scattering.

12.4. Random laser based on dye-doped latex nanoparticles used for speckle-free imaging. Properties and characterization

In our study, a RL composed of dye-doped latex nanoparticles was used as a probe laser for speckle-free imaging. A solution of Rhodamine B in Ethanol with a concentration of [RhB] = 5 mM was used as an amplifying medium. Latex nanoparticles of 325 nm diameter in colloidal suspension at a concentration of [NP] = 4.10^{15} particles per litre (p/L) acted as a scatterer in the amplifying medium. This solution was then poured into a 1x10 quartz cuvette and used as a RL. Pumping of the amplifying medium was performed by a 532 nm doubled YAG laser (Q-smart 450, Quantel Laser). The laser pump pulse duration is 6 ns, operating at 10 Hz, and the maximum average power of the system is 2.2 W. The output power of the laser head can be manually controlled using a power attenuator.

The concentration of nanoparticles in the amplifying medium is such that the penetration of light into the medium is very limited. Indeed, by analogy with Beer Lambert's law, the attenuation of the light intensity I at position l in a diffusive medium can be described by

$$I(l) = I_0 e^{-l/l_d} \quad (1)$$

Where I_0 is the light intensity at position $l = 0$ (i.e., before penetrating the sample) and l_d, the characteristic length of penetration into the scattering medium defined by

$$l_d = \frac{1}{[NP]\sigma_{np}} \quad (2)$$

where σ_{np} is the effective cross-sectional area of a 325 nm diameter latex particle and [NP] the nanoparticle concentration in the solution. Mie's theory can then give the effective cross-section of light scattering at 532 nm by a 352 nm latex nanoparticle in Ethanol, knowing the refractive index of the particle. We then have $\sigma_{np} = 6.10^{-10} cm^2$. The characteristic length of penetration into the diffusive medium can be estimated as $l_d \sim 5\,\mu m$. It corresponds to the average distance between scattering events. In other words, after a few tens of micrometers, the solution is completely opaque. The volume of the pumped amplifying medium is, therefore, very small and localized on the surface of the cuvette.

12.4.1. Properties

The main properties of the RL were explored in order to determine the key elements for optimal illumination conditions for optical microscopy. As previously mentioned, the volume of the pumped amplifying medium is located on the surface of the cuvette. The RL emission is then only in the half-space outside the solution with a

maximum emission perpendicular to the cuvette, as shown in Figure 12.7. For this reason, the attack of the pump beam on the cuvette of the RL is done with a large angle, and the collection of the emitted signal is done according to the normal of the cuvette directly. The physical quantity to characterize the power supplied to the amplifying medium by the pump is the luminous fluence. It is defined as the energy per laser pulse per surface element (given in Joule per square centimetre - $J.cm^{-2}$) and is independent of the pulse duration.

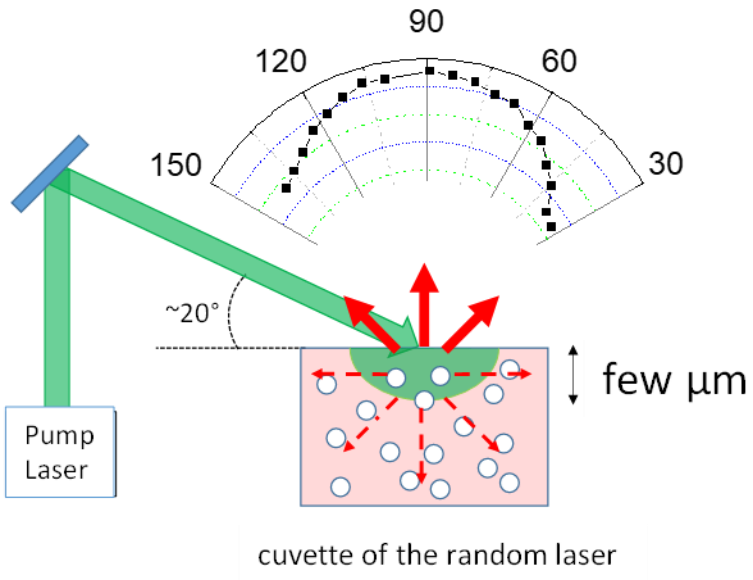

Figure 12.7 Schematic diagram showing the anisotropy of the random laser emission. The graph shows the maximum of the random laser emission as a function of the collection angle.

The emission spectra of the amplifying medium in the presence or absence of latex particles are given in Figure 12.8a. Several characteristic phenomena are visible very clearly. For an identical pump fluence, we can observe an amplification of the emission signal and a narrowing of the emission band centred at 595 nm in the presence of nanoparticles. In addition, a pumping threshold is observed below which

the amplification and narrowing of the emission band are not visible (Figure 12.8b). Amplification, wavelength selection, and the presence of a pumping threshold are characteristics of laser emissions. Figure 12.8c shows the evolution of the emission spectrum as a function of pump fluence. For high pump fluences, we can see the appearance of a second laser peak at 615 nm. This second peak can be attributed to the emission of Rhodamine B dimers present in the solution in the amplifying medium.[74] The first laser threshold is estimated to be 3 mJ.cm^{-2}, and the second peak is estimated to be 100 mJ.cm^{-2}.

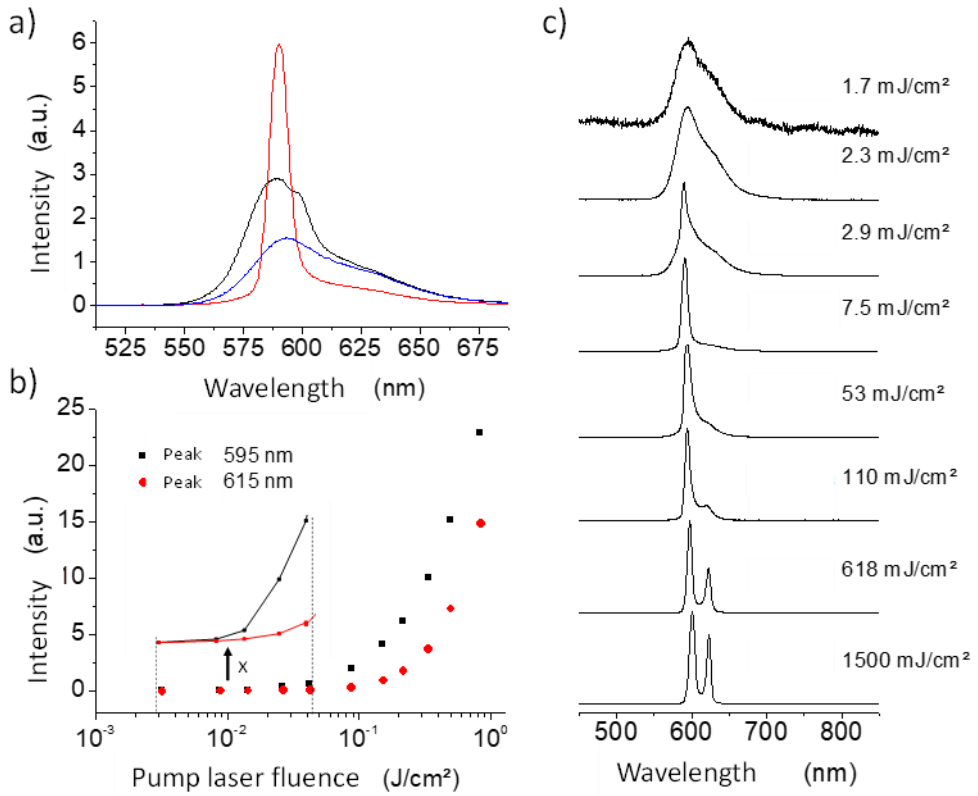

Figure 12.8 (a) Emission spectra of (black) a 5 mM Rhodamine B solution pumped at 7.5 mJ/cm², (blue) a Rhodamine B solution in the presence of nanoparticles pumped at 2.3 mJ/cm² (below the laser threshold) and (red) a Rhodamine B solution in the presence of nanoparticles pumped at 7. 5 mJ/cm² (above the laser threshold) divided by a factor of 10. (b) Evolution of the intensity maximum at 595 nm and 615

nm of the random laser emission as a function of the pump fluence. (c) Evolution of the random laser emission spectrum for different pump fluences.

The intensity of the RL emission as a function of pump fluence is given for different concentrations of latex nanoparticles suspended in the amplifying medium in Figure 12.9a. The existence of a laser threshold is clearly visible when the amplifying medium has diffusive properties. This threshold can be defined more precisely by the width at half height of the emission spectrum, which drops sharply from 60 nm to about 8 nm (Figure 12.9b). It is then shown that the Rhodamine B solution in the absence of nanoparticles does not show any characteristic signs of amplification or narrowing of its emission spectrum when the laser fluence of the pump increases. Moreover, it is noted that the higher the nanoparticle concentration, the greater the laser amplification. Intuitively, we understand that if the number of scattering elements increases in the volume of the pumped amplifying medium, the number of scattering events increases. A photon will then remain trapped in the amplifying medium for a longer time, thus increasing the total gain of the RL.

Similarly, the larger the size of the nanoparticle, the more efficient the scattering will be and the more amplified the emission will be (Figure 12.9c). In addition, the dependence of the RL emission on the chromophore concentration has been studied (Figure 12.9e). It is then shown that the higher the chromophore concentration, the higher the RL efficiency.

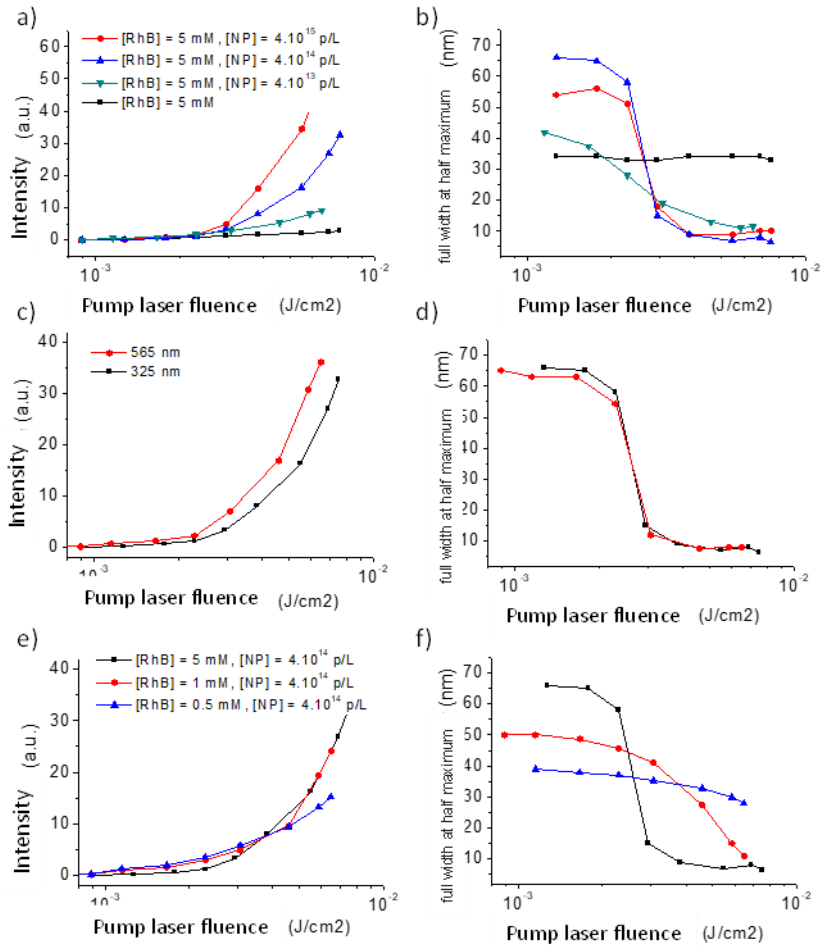

Figure 12.9 (a, c, e) Intensity and (b, d, f) half-height width of the random laser emission spectrum as a function of pump fluence for different amplifier media. (a, b) as a function of nanoparticle concentration, (c, d) as a function of NP size, and (e, f) as a function of dye concentration.

Figure 12.10 shows the impact of the pump laser spot size on the laser threshold of the amplifying medium. At constant power, as the focal spot diameter decreases, the light fluence per laser pulse increases. However, the volume of the pumped amplifying medium also decreases, and therefore, the laser threshold is more difficult to reach. A balance between pump fluence and signal intensity must then be found to optimize the RL emission.

Finally, it should be noted that the duration of the doubled YAG laser pulse used for pumping (6 ns) is longer than the lifetime of the excited state of the chromophore used as an amplifying medium (the lifetime of Rhodamine B is about 2.5 ns in Ethanol). Thus, the timing of the RL pulse is close to that of the pump. However, for pumping by a shorter laser pulse (typically picosecond), the duration of the RL pulse is not trivial and requires further study.[75]

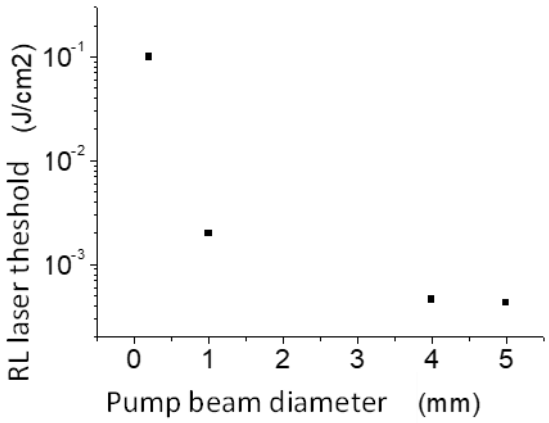

Figure 12.10 Random laser threshold as a function of the size of the laser focal spot used to pump the amplifying medium.

12.4.2. Implementing random laser to pump-probe optical microscopy

The laser beam used for pumping the RL attacks the RL cuvette at a wide angle and is slightly focused to obtain a focal spot of 3 mm on the RL cuvette. In order to collect the RL emission, a large aspherical condenser lens and short focal length were used. This collection lens is placed 60 mm from the RL cuvette so that the light collected in the microscope can be injected towards the condenser for illumination alignment. For laser pump energy values well above the laser threshold, the RL pulse energy varies linearly with the pump pulse energy. The efficiency of the RL is then estimated at 4%. Given the small volume of the pumped amplifying medium, the

total volume of the cuvette, and the high stability of the solution used, the lifetime of the RL is very long: over the whole duration of the experiments carried out, we did not observe any loss of emission intensity of the RL even when operating at 10 Hz (pump rate), as long as the solution was regularly mixed, sealed and properly stored.

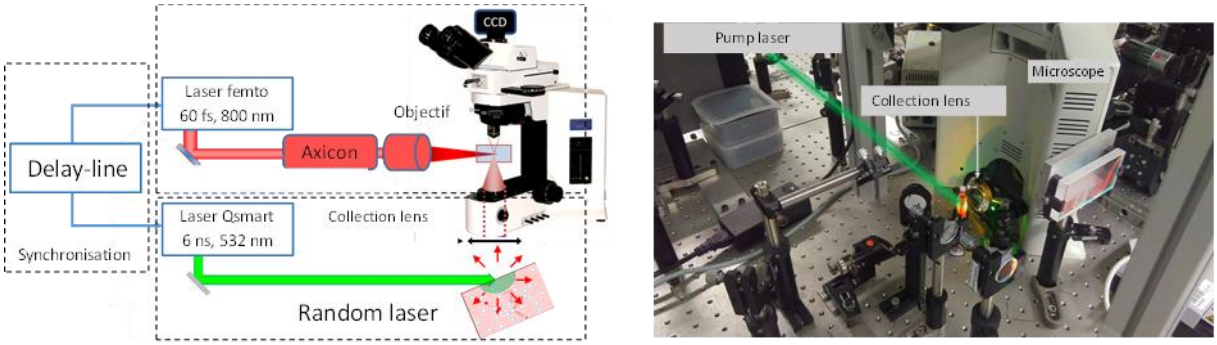

Figure 12.11 Schematic representation of the newly developed experimental set-up. And the photograph of the implementation of the random laser as an illumination source for optical microscopy.

The synchronization of the Ti: Sapphire laser pulses used to generate the plasma and the frequency-doubled YAG laser used to pump the RL is provided by an electronic delay line. Thus, the two pulses can be triggered in a synchronized manner with a jitter of about 50 ns with a possible delay of 0 to 100 ms (with a minimum delay of 100 ns), allowing for significant dynamic exploration. Figure 12.11 shows a schematic representation of the newly developed experimental setup.

12.4.3. Probing microbubble dynamics with time-resolved microscopy with random lasers

In order to observe the microbubble by RL imaging, the illumination delay is initially set at 100 ns. Figure 12.12 shows the exact image of the microbubble about 100 ns after the plasma formation. This image was acquired following a single laser shot

into the water with a pulse duration of 4 ps and energy of 5 µJ in a narrow focus condition. The absence of speckles is direct evidence of the spatial non-coherence of the RL illumination. The contours of the observed bubble are very well defined (as compared with the Image of the micrometric bubble displayed in Figure 12.2). The temporality of the illumination is of the order of a few nanoseconds, which remains small compared to the dynamics of the bubble.

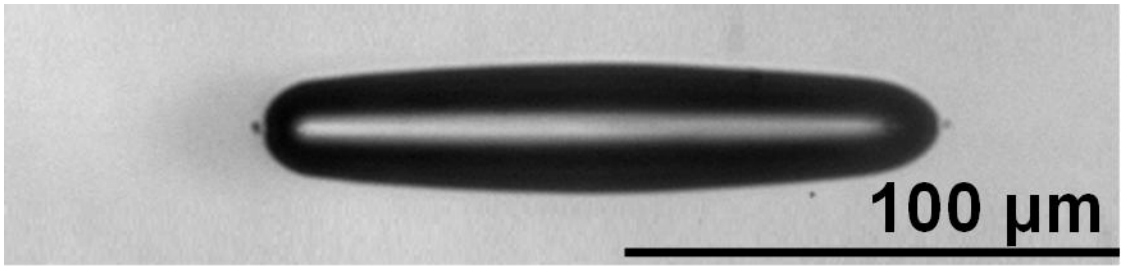

Figure 12.12 Image of the micrometric bubble generated by nano-cavitation 100 ns after the laser pulse. The acquisition is performed after a single laser shot.

A dark surface well defines the solvent-gas interface of the bubble. The core of the bubble appears to be lighter than the background of the image. This may be due to a converging lens effect of the bubble surface, which is outside the focal plane of the image. Figure 12.13 shows the existence of the cavitation threshold for femtosecond excitation at 120 fs and picosecond at 4 ps, characterized by an observation at about 100 ns. The quality of the images makes it possible to see very clearly the instabilities of the microbubble at its surface for high energies. The values of these cavitation thresholds for sub-picosecond and picosecond excitations are then of the order of those determined previously (1 µJ and 2.3 µJ respectively), validating this illumination technique. Using the electronic delay line, the complete microbubble dynamics could be explored in different solvents for single laser shots. Figure 12.14 shows the dynamics of microbubbles generated by a 4 ps laser pulse with an energy

of 5 μJ in a narrow focus condition in water and in a high-viscosity solvent: Ethylene Glycol.

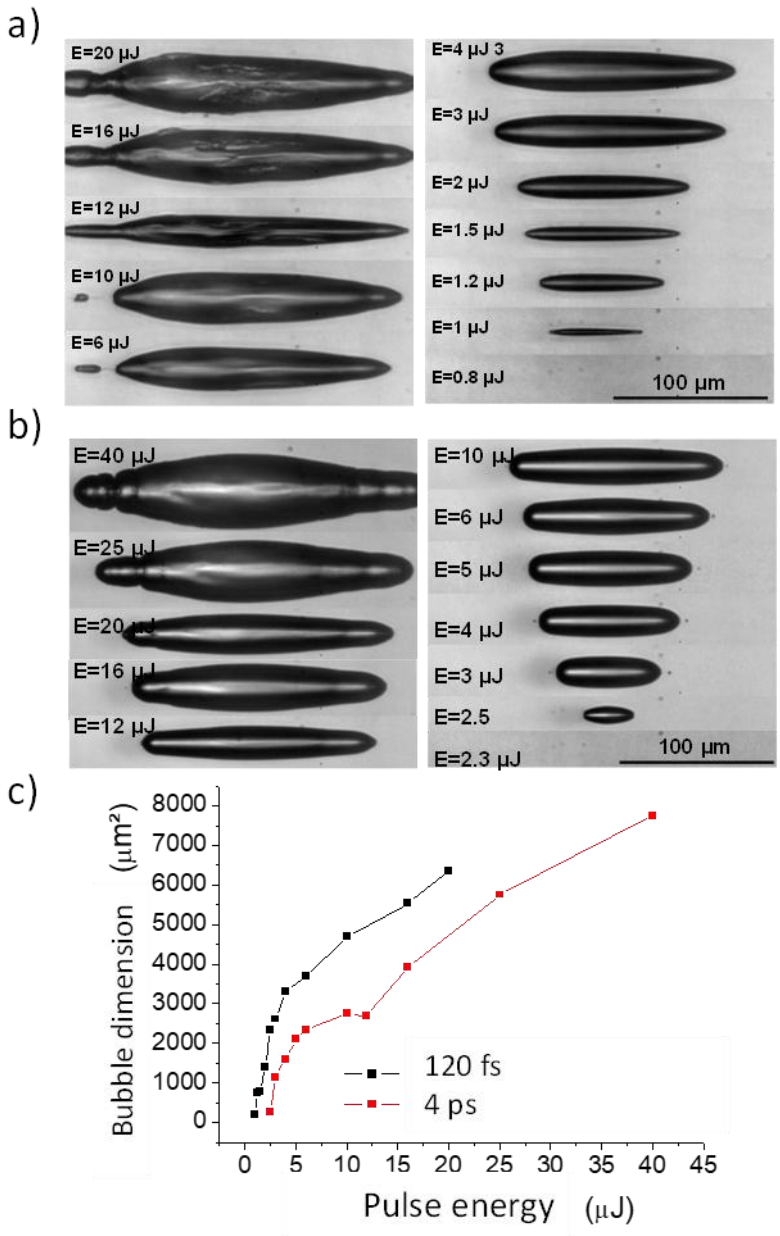

Figure 12.13 Images of the micrometer bubble at 100 ns after the laser pulse for different laser energies for a pulse duration of (a) 120 fs and (b) 4 ps. (c) Dimension of the bubble projection as a function of the laser pulse energy for these two different pulse durations.

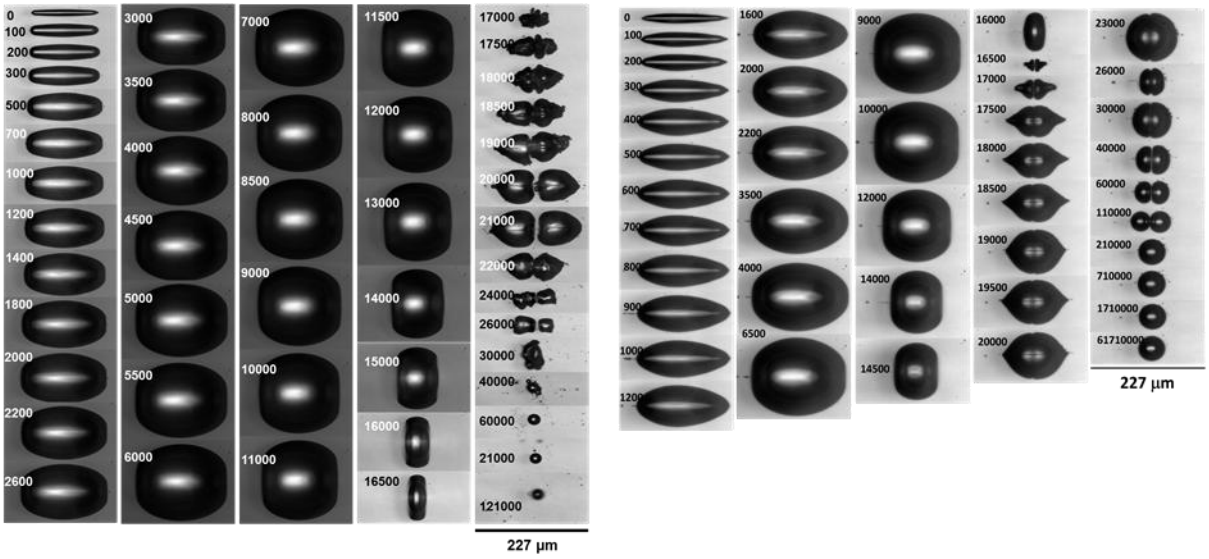

Figure 12.14 Dynamics of a microbubble generated in water (left panel) and in ethylene glycol (right panel) by a 4 ps laser pulse of energy 5 µJ. The delay between laser excitation and image acquisition is given in nanoseconds in each image.

Whatever solvent is used, the expansion and collapse of the microbubble, followed by one or more bounces, characteristic of cavitation-generated bubbles, are observed.[76,77] Moreover, although these images are recorded with new generated bubbles at each time, the small deviation of the microbubble size evolution confirms once again the stability of laser cavitation generation. The geometry of the bubble generated by the Bessel beam imposes an inhomogeneous spatial expansion of the bubble. During the expansion phase, the dimension of the major axis of the bubble remains unchanged: the microbubble expands only along its transverse axis until it reaches a quasi-spherical shape when its volume is maximum. Conversely, the microbubble collapses along the longitudinal axis. During the second oscillation, the bubble undergoes fission: the intense hydrodynamic forces brought into play by the asymmetry of the bubble give rise to two new microbubbles along the longitudinal axis, which then continue their expansion-collapse series. Despite the random nature

of this fission, it is observed at each laser shot. When the viscosity of the solvent is high, the contours of the objects resulting from this fission are better defined and appear less chaotic. We can consider the total surface of the object projected in the observation plane as a dimensional parameter of these objects whose shape evolves over time. In this way, Figure 12.15 gives the dynamics of the microbubble over time in water and Ethylene Glycol. The lifetime of the microbubble corresponding to the time of the first oscillation following the formation of the bubble is estimated at 15.3 µs in water and 16.4 µs in Ethylene Glycol. Then, the oscillations continue, reducing the size of the initial bubble until a stable bubble survives and emerges from the focal plane of the microscope objective after a few milliseconds.

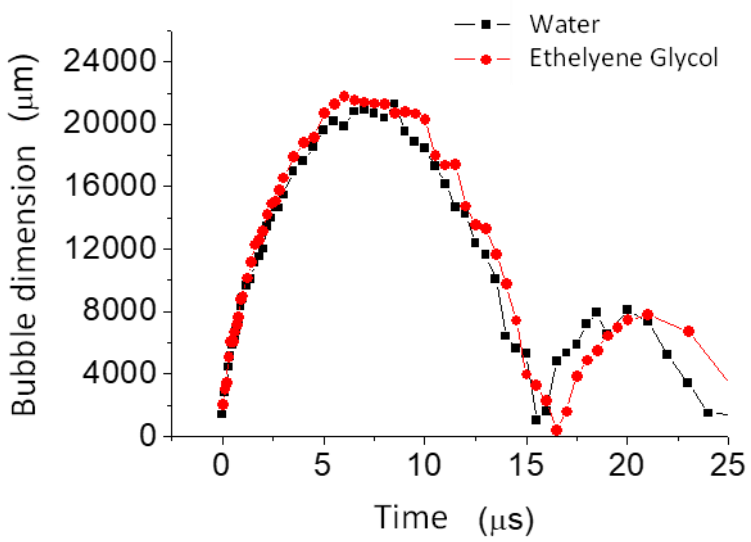

Figure 12.15 Evolution of the bubble size as a function of time for a microbubble generated by a 4 ps laser pulse of energy 5 µJ.

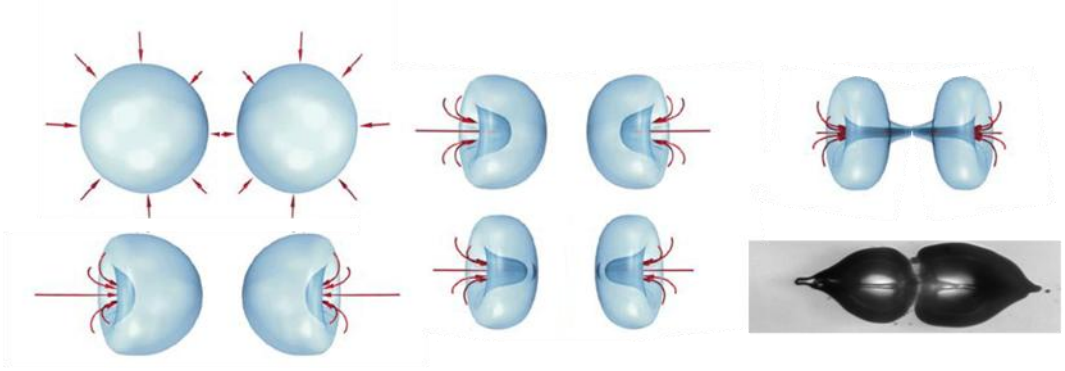

Figure 12.16 illustration (schematic and experimental profiles) of internal micrometric jets observed during the collapse phase.

Internal micrometric jets can also be observed during the collapse phase, as shown in Figure 12.16. These micro-jets are characteristic of bubbles generated by cavitation (laser-induced or not) and are attributed to be responsible for the material damage often accompanying cavitation phenomena.

12.4.4. Other studies using time-resolved microscopy with random lasers

As seen in the previous section, two vital features of RL are brightness and low coherence. Due to these properties, speckle-less imaging is possible. The bright, low-coherence narrowband illumination source has the potential to acquire high-quality speckle-free images, providing information on the amplitude and the phase of the object at the same time. This illumination method significantly increases the dynamical range of the image and the signal-to-noise ratio, allowing us to take full advantage of the optical resolution of the microscope with time resolution. Indeed, Cao and coworkers quantitatively showed that images generated with RL illumination exhibit superior quality than images generated with spatially coherent illumination. [29] Speckle-free bioimaging is a very powerful application of paramount importance. For

instance High contrast dental imaging using a near-infrared random fiber laser in a backscattering imaging method was demonstrated by Anderson S. L. Gomes.[78]

In addition to (bio)imaging, optical imaging of fast events and processes is essential for understanding dynamics of complex systems. Vladislav V. Yakovlev and colleagues demonstrated the use of random Raman lasing as a novel imaging light source with unprecedented brightness for a speckle-free and narrowband light source.[79]

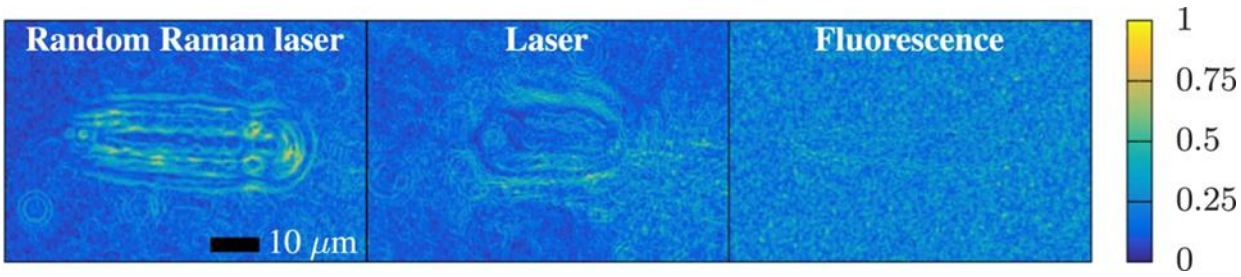

Figure 12.17 Images of laser induced breakdown in water after 2 ns delay passed through a Sobel filter to compute the gradient. The magnitude of the gradient is shown. This kind of filter is commonly used in image processing for edge detection as it highlights areas where contrast is high. Thus, in this case it is being used to highlight the higher degree of detail captured by random Raman lasing due to the lack of speckle while maintaining sufficient temporal resolution to capture the laser induced breakdown event.

To improve the quality of these images, a Sobel filter was proposed, which computes the gradient of the image to the images taken with each light source. The results very clearly highlight the resolution of small-scale features in the center of the breakdown under random Raman laser illumination that are not well resolved by the laser and are totally non-existent with the fluorescence source (see Figure 12.17). Alexandre Mermillod-Blondin et al. [37] did pioneering work in the field of time-resolved

microscopy with RLs. The authors utilized a RL to illuminate a commercially available microscope that enables single-exposure, speckle-free time-resolved imaging. They applied this method to the monitoring of fs-laser-induced microdot formation in bulk a-SIO_2. Time-resolved investigations show that microdot formation lasts over several microseconds after laser excitation.

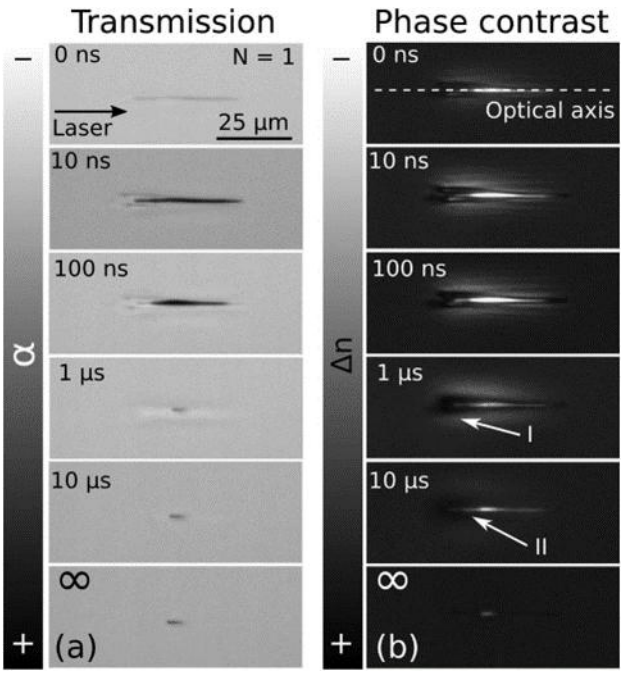

Figure 12.18 (a) Optical transmission (OTM) and (b) phase contrast (PCM) time-resolved micrographs of the laser-induced microdot. A random laser provided the illumination source.

In Figure 12.18, the time-resolved snapshots (measurements in OTM and in PCM) of the microdot formation presented are shown. The background illumination is very uniform in both cases, and the object of interest stands out with a very satisfying contrast.

Recently, Razvan Stoian and coworkers described the evolution of ultrafast-laser-excited bulk fused silica over the entire relaxation range in one-dimensional geometries fixed by non-diffractive beams. [80] High-resolution speckle-free

microscopy, using RLs (dye-doped nanoparticles) as probe beams, was used to image optical signatures associated to structural transformations until the evolution stops. Multi-scale imaging indicates characteristic timescales for plasma decay, heat diffusion, and void cavitation, pointing out key mechanisms of material transformation on the nanoscale in a range of processing conditions.

12.5. Concluding remarks. Challenges and opportunities

RLs have shown great potential for use in various imaging applications. They are ideal for use in scattering environments such as biological imaging or imaging through atmospheric turbulence. The high degree of scattering in these environments requires a source with low spatial coherence and brighter illumination than can be achieved with existing spatially incoherent sources. By meeting these two requirements, RL sources can enable parallel (full-field) imaging in scattering environments. In addition, RLs offer the unique ability to provide tunable spatial coherence, which opens up the possibility of optimizing the illumination source for specific imaging applications. This tunable spatial coherence can help prevent speckle formation, which is a common problem in imaging. It makes RLs an attractive alternative to traditional light sources such as LEDs or conventional lasers. One of the significant challenges facing the use of RLs in imaging is their low efficiency. Efforts are being made to improve the efficiency of these lasers to make them more practical for use in imaging applications. Another challenge is the stability of these lasers, which can be affected by changes in temperature or other environmental factors.

Despite these challenges, there are many exciting future perspectives for the use of RLs in imaging. Researchers are exploring new materials and fabrication techniques

to create more complex and functional RL structures. They are also working to improve the brightness and coherence control of RL sources. In addition, new imaging techniques that take advantage of the unique properties of RLs are being developed. Overall, the future of random lasing research looks promising, with potential applications in a wide range of fields such as biology, medicine, and remote sensing. Further developments in RL technology could lead to new imaging technologies that are more efficient, stable, and adaptable to specific imaging applications.

ACKNOWLEDGEMENTS

NP and NK acknowledge the financial support from BRNS-DAE, Govt. of India, DST for funding through the INSPIRE scheme, PURSE PII, FIST and Nano Mission programs, UGC, Govt. of India for funding through SAP-DRS and Innovative program, SAIF-MGU. RA and NK acknowledge CNRS for funding through International Emerging Actions between Institut Lumière Matière, CNRS, France, and Mahatma Gandhi University, India. RA acknowledges the financial support of the Université de Lyon through Programme Avenir Lyon Saint-Etienne (PALSE project ERTIGO) and the Program “Investissements d’Avenir” (ANR-11-IDEX-0007).

References

1L. Xinju, X. Lan and C. Huamin, Laser technology, CRC press, 2010.

2M. Ozaki, M. Kasano, D. Ganzke, W. Haase and K. Yoshino, Adv. Mater., 2002, 14, 306–309.

3T. H. Dudok and Y. A. Nastishin, Ukr. J. Phys. Opt., 2014, 47–67.

4Y. A. Nastishin and T. H. Dudok, Ukr. J. Phys. Opt., 2013, 146–170.

5H. Finkelmann, S. T. Kim, A. Munoz, P. Palffy-Muhoray and B. Taheri, Adv. Mater., 2001, 13, 1069–1072.

6V. Letokhov, Sov. J. Exp. Theor. Phys., 1968, 26, 835.

7V. M. Markushev, V. F. Zolin and C. M. Briskina, 1986, 281, 2–5.

8B. Garc\'\ia-Ramiro, M. A. Illarramendi, S. Garc\'\ia-Revilla, R. Balda, D. Levy, M. Zayat and J. Fernández, Appl. Phys. B, 2014, 117, 1135–1140.

9S. García-Revilla, M. Zayac, R. Balda, M. Al-Saleh, D. Levy and J. Fernández, Opt. Express, 2009, 17, 13202.

10J. G. Câmara, D. M. da Silva, L. R. P. Kassab, C. B. de Araújo and A. S. L. Gomes, J. Lumin., 2021, 233, 117936.

11F. R. Lamastra, R. De Angelis, A. Antonucci, D. Salvatori, P. Prosposito, M. Casalboni, R. Congestri, S. Melino and F. Nanni, RSC Adv., 2014, 4, 61809–61816.

12V. S. Gummaluri, R. Gayathri, C. Vijayan and V. M. Murukeshan, J. Opt. (United Kingdom), , DOI:10.1088/2040-8986/ab896b.

13S. Krämmer, C. Vannahme, C. L. C. Smith, T. Grossmann, M. Jenne, S. Schierle, L. Jørgensen, I. S. Chronakis, A. Kristensen and H. Kalt, Adv. Mater., 2014, 26, 8096–8100.

14G. Dai, L. Wang and L. Deng, Opt. Mater. Express, 2020, 10, 68–75.

15Q. Song, S. Xiao, Z. Xu, J. Liu, X. Sun, V. Drachev, V. M. Shalaev, O. Akkus and Y. L. Kim, Opt. Lett., 2010, 35, 1425–1427.

16Y. Wang, Z. Duan, Z. Qiu, P. Zhang, J. Wu, D. Zhang and T. Xiang, Sci. Rep., 2017, 7, 1–7.

17R. Gayathri, C. S. Suchand Sandeep, C. Vijayan and V. M. Murukeshan, Opt. InfoBase Conf. Pap., 2021, 2021, 5–7.

18R. C. Polson and Z. V Vardeny, , DOI:10.1088/2040-8978/12/2/024010.

19R. C. Polson and Z. V. Vardeny, Appl. Phys. Lett., 2004, 85, 1289–1291.

20X. Yang, C. Gong, Y. Liu, Y. Rao, M. Smietana and Y. Gong, 2021, 11, 262–278.

21M. Gaio, S. Caixeiro, B. Marelli, F. G. Omenetto and R. Sapienza, Phys. Rev. Appl., 2017, 7, 34005.

22R. Gayathri, C. S. S. Sandeep, K. Ahmad, C. Vijayan and V. M. Murukeshan, Opt. InfoBase Conf. Pap., 2021, 2021, 6–7.

23B. Redding, M. A. Choma and H. Cao, Nat. Photonics, 2012, 6, 355–359.

24D. Zhang, Y. Wang, J. Tang and H. Mu, J. Appl. Phys., , DOI:10.1063/1.5095834.

25C. Y. Su, C. F. Hou, Y. T. Hsu, H. Y. Lin, Y. M. Liao, T. Y. Lin and Y. F. Chen, ACS Appl. Mater. Interfaces, 2020, 12, 49122–49129.

26X. Shi, Y. Bian, J. Tong, D. Liu, J. Zhou and Z. Wang, Opt. Express, 2020, 28, 13576–13585.

27K. C. Jorge, M. A. Alvarado, E. G. Melo, M. N. P. Carreño, M. I. Alayo and N. U. Wetter, Appl. Opt., 2016, 55, 5393–5398.

28B. Redding, A. Cerjan, X. Huang, M. Larry, A. D. Stone and M. A. Choma, 2015, 112, 1304–1309.

29B. Redding, M. A. Choma and H. Cao, Nat. Photonics, , DOI:10.1038/nphoton.2012.162.

30T.-H. Yang, C.-W. Chen, H.-C. Jau, T.-M. Feng, C.-W. Wu, C.-T. Wang and T.-H. Lin, Appl. Phys. Lett., 2019, 114, 191105.

31M. K. Bhuyan, F. Courvoisier, P. A. Lacourt, M. Jacquot, R. Salut, L. Furfaro and J. M. Dudley, Appl. Phys. Lett., 2010, 97, 1–4.

32M. K. Bhuyan, A. Soleilhac, M. Somayaji, T. E. Itina, R. Antoine and R. Stoian, Sci. Rep., 2018, 8, 1–12.

33M. Duocastella and C. B. Arnold, Laser Photon. Rev., 2012, 6, 607–621.

34J. Durnin, J. J. Miceli Jr and J. H. Eberly, Phys. Rev. Lett., 1987, 58, 1499.

35M. K. Bhuyan, F. Courvoisier, P. A. Lacourt, M. Jacquot, R. Salut, L. Furfaro and J. M. Dudley, Appl. Phys. Lett., 2010, 97, 81102.

36I. Toytman, D. Simanovski and D. Palanker, Opt. Express, 2010, 18, 24688–24698.

37A. Mermillod-Blondin, H. Mentzel and A. Rosenfeld, Opt. Lett., 2013, 38, 4112–4115.

38N. Padiyakkuth, S. Thomas, R. Antoine and N. Kalarikkal, Mater. Adv., 2022, 3, 6687–6706.

39R. V Ambartsumyan, N. G. Basov, P. G. Kryukov and V. S. Letokhov, Sov. Phys. JETP, 1967, 24, 481–485.

40H. Cao, J. Y. Xu, Y. Ling, A. L. Burin, E. W. Seeling, X. Liu and R. P. H. Chang, IEEE J. Sel. Top. Quantum Electron., 2003.

41H. Cao, J. Phys. A. Math. Gen., 2005, 38, 10497–10535.

42D. S. Wiersma, Nat. Phys., 2008, 4, 359–367.

43J. Tian, G. Weng, Y. Wang, X. Hu, S. Chen and J. Chu, ACS Appl. Nano Mater., 2019, 2, 1909–1919.

44V. M. Markushev, M. V. Ryzhkov, C. M. Briskina, H. Cao, L. A. Zadorozhnaya, E. I. Givargisov, H. Zhong, S.-W. Wang and W. Lu, Laser Phys., , DOI:10.1134/s1054660x07090010.

45H. Fujiwara, T. Suzuki, R. Niyuki and K. Sasaki, Opt. InfoBase Conf. Pap., , DOI:10.1364/ACOFT.2016.JT4A.9.

46A. T. Ali, W. Maryam, Y. W. Huang, H. C. Hsu, N. M. Ahmed, N. Zainal and M. S. Jameel, Opt. Laser Technol., 2022, 147, 107633.

47H. Y. Yang, S. F. Yu, J. Yan and L. D. Zhang, Nanoscale Res. Lett., 2010, 5, 809–812.

48C. Kim, D. V. Martyshkin, V. V. Fedorov and S. B. Mirov, Opt. Commun., 2009, 282, 2049–2052.

49H. Y. Yang, S. F. Yu, J. Yan and L. D. Zhang, Nanoscale Res. Lett., 2010, 5, 809–812.

50M. Rashidi, T. Haggren, Z. Su, C. Jagadish, S. Mokkapati and H. H. Tan, Nano Lett., 2021, 21, 3901–3907.

51T. Nakamura, T. Takahashi and S. Adachi, Phys. Rev. B - Condens. Matter Mater. Phys., 2010, 81, 1–6.

52G. Zhu, C. E. Small and M. A. Noginov, Opt. Lett., 2008, 33, 920.

53E. Jiménez-Villar, I. F. Da Silva, V. Mestre, N. U. Wetter, C. Lopez, P. C. De Oliveira, W. M. Faustino and G. F. De Sá, ACS Omega, 2017, 2, 2415–2421.

54E. Jimenez-Villar, V. Mestre, W. S. Martins, G. F. Basso, I. F. Da Silva and G. F. De Sá, Mater. Today Proc., 2017, 4, 11570–11579.

55H. W. Shin, S. Y. Cho, K. H. Choi, S. L. Oh and Y. R. Kim, Appl. Phys. Lett., 2006, 88, 2–5.

56A. K. Tiwari, S. Shaik and S. A. Ramakrishna, Appl. Phys. B Lasers Opt., 2018, 124, 1–8.

57D. Cao, D. Huang, X. Zhang, S. Zeng, J. Parbey, S. Liu, C. Wang, T. Yi and T. Li, Laser Phys., 2018, 28, 25801.

58A. Ghasempour Ardakani and P. Rafieipour, Phys. B Condens. Matter, 2018, 546, 49–53.

59N. Padiyakkuth, R. Antoine and N. Kalarikkal, Opt. Mater. (Amst)., 2022, 129, 112408.

60T. Naruta, T. Akita, Y. Uchida, D. Lisjak, A. Mertelj and N. Nishiyama, Opt. Express, 2019, 27, 24426.

61H. T. Dai, M. N. Gao, Y. X. Xue, A. X. Xiao, A. Ahmad, Z. Mohamed, C. L. Liu, Q. Lu and S. Z. Feng, AIP Adv., , DOI:10.1063/1.5120438.

62N. Padiyakkuth, R. Antoine and N. Kalarikkal, J. Lumin., 2022, 252, 119296.

63Z. Meng, Y. Yang and Y. Wan, Indian J. Phys., , DOI:10.1007/s12648-021-02109-x.

64S. Perumbilavil, A. Piccardi, O. Buchnev, M. Kauranen, G. Strangi and G. Assanto, Opt. Express, 2017, 25, 4672.

65L. Ye, C. Zhao, Y. Feng, B. Gu, Y. Cui and Y. Lu, Nanoscale Res. Lett., 2017, 12, 1–8.

66A. Piccardi, S. Perumbilavil, M. Kauranen, G. Strangi and G. Assanto, in PHOTOPTICS 2019 - Proceedings of the 7th International Conference on Photonics, Optics and Laser Technology, 2019.

67Y. Sakurayama, T. Onodera, Y. Araki, T. Wada and H. Oikawa, RSC Adv., 2021, 11, 32030–32037.

68X. Meng, J. Ma, K. Xie, L. Hong, J. Zhang and Z. Hu, Opt. Mater. (Amst)., , DOI:10.1016/j.optmat.2021.111027.

69N. I. M. Tazri, O. L. Muskens, M. K. Shakfa and W. Maryam, J. Appl. Phys., 2019, 125, 0–5.

70H. Zhang, G. Feng, H. Zhang, C. Yang, J. Yin and S. Zhou, Results Phys., 2017, 7, 2968–2972.

71N. Rosli, M. M. Halim, M. R. Hashim, H. C. Hsu and J. Y. Zhuang, 2021, 2, 1–7.

72C. C. Wang, M. Kataria, H. I. Lin, A. Nain, H. Y. Lin, C. R. Paul Inbaraj, Y. M. Liao, A. Thakran, H. T. Chang, F. G. Tseng, Y. P. Hsieh and Y. F. Chen, ACS Photonics, 2021, 8, 3051–3060.

73E. Mendicuti, O. Käferlein and C. García-Segundo, Opt. Lett., 2021, 46, 274–277.

74C. T. Dominguez, E. de Lima, P. C. de Oliveira and F. L. Arbeloa, Chem. Phys. Lett., 2008, 464, 245–248.

75C. M. Soukoulis, X. Jiang, J. Y. Xu and H. Cao, Phys. Rev. B, 2002, 65, 41103.

76C. E. Brennen, Cavitation and bubble dynamics, Cambridge university press, 2014.

77I. Akhatov, O. Lindau, A. Topolnikov, R. Mettin, N. Vakhitova and W. Lauterborn, Phys. Fluids, 2001, 13, 2805–2819.

78J. Y. Guo, W. L. Zhang, Y. J. Rao, H. H. Zhang, R. Ma, D. S. Lopes, I. C. X. Lins and A. S. L. Gomes, OSA Contin., 2020, 3, 759.

79B. H. Hokr, J. V Thompson, J. N. Bixler, D. T. Nodurft, G. D. Noojin, B. Redding, R. J. Thomas, H. Cao, B. A. Rockwell, M. O. Scully and others, Sci. Rep., 2017, 7, 1–7.

80M. Somayaji, M. K. Bhuyan, F. Bourquard and P. K. Velpula, Sci. Rep., 2020, 1–9.

FIGURE AND TABLE CAPTIONS

Figure 12.1 (a) Experimental setup with a time-resolved pump-probe observation. Simulation of the intensity of a Bessel beam projected (b) along the propagation axis and (c) in a plane transverse to the propagation axis of the laser beam.

Figure 12.2 Image of the micrometric bubble obtained after a single laser shot (a single acquisition) and averaged over 50 shots, illustrating the problem of spatial and temporal coherence of the probe beam inducing “speckles”.

Figure 12.3 Graphical representation of the problem of illumination techniques for optical microscopy. Adapted from [B. Redding, M. A. Choma, and H. Cao, “Speckle-free laser imaging using random laser illumination,” Nat Phot., vol. 6, no. 6, pp. 355–359, Jun. 2012].

Figure 12.4 Description of the mechanisms involved in the laser process with a simplified Jablonski diagram for a four-level system

Figure 12.5 On the left, the principle of a “classical” laser. Feedback is provided by an optical cavity. On the right, the principle of a random laser. The feedback is provided by multiple and successive scatterings in the amplifying medium [38].

Figure 12.6 Laser pumping experiment of hydrogel attached to the hand (Reproduced from ref. 59, with permission from [Elsevier]).

Figure 12.7 Schematic diagram showing the anisotropy of the random laser emission. The graph shows the maximum of the random laser emission as a function of the collection angle.

Figure 12.8 (a) Emission spectra of (black) a 5 mM Rhodamine B solution pumped at 7.5 mJ/cm², (blue) a Rhodamine B solution in the presence of nanoparticles pumped at 2.3 mJ/cm² (below the laser threshold) and (red) a Rhodamine B solution in the presence of nanoparticles pumped at 7. 5 mJ/cm² (above the laser threshold) divided by a factor of 10. (b) Evolution of the intensity maximum at 595 nm and 615 nm of the random laser emission as a function of the pump fluence. (c) Evolution of the random laser emission spectrum for different pump fluences.

Figure 12.9 (a, c, e) Intensity and (b, d, f) half-height width of the random laser emission spectrum as a function of pump fluence for different amplifier media. (a, b)

as a function of nanoparticle concentration, (c, d) as a function of NP size, and (e, f) as a function of dye concentration.

Figure 12.10 Random laser threshold as a function of the size of the laser focal spot used to pump the amplifying medium.

Figure 12.11 Schematic representation of the newly developed experimental set-up. And photograph of the implementation of the random laser as an illumination source for optical microscopy.

Figure 12.12 Image of the micrometric bubble generated by nano-cavitation 100 ns after the laser pulse. The acquisition is performed after a single laser shot.

Figure 12.13 Images of the micrometer bubble at 100 ns after the laser pulse for different laser energies for a pulse duration of (a) 120 fs and (b) 4 ps. (c) Dimension of the bubble projection as a function of the laser pulse energy for these two different pulse durations.

Figure 12.14 Dynamics of a microbubble generated in water (left panel) and in ethylene glycol (right panel) by a 4 ps laser pulse of energy 5 µJ. The delay between laser excitation and image acquisition is given in nanoseconds in each image

Figure 12.15 Evolution of the bubble size as a function of time for a microbubble generated by a 4 ps laser pulse of energy 5 µJ.

Figure 12.16 Représentation de l'effondrement d'une bulle générée par cavitation mettant en évidence la présence de jet micrométrique interne

Figure 12.17 Images of laser induced breakdown in water after 2 ns delay passed through a Sobel filter to compute the gradient. The magnitude of the gradient is shown. This kind of filter is commonly used in image processing for edge detection as it highlights areas where contrast is high. Thus, in this case it is being used to highlight the higher degree of detail captured by random Raman lasing due to the

lack of speckle while maintaining sufficient temporal resolution to capture the laser induced breakdown event.

Figure 12.18 (a) Optical transmission (OTM) and (b) phase contrast (PCM) time-resolved micrographs of the laser-induced microdot. A random laser provided the illumination source

ABBREVIATIONS